

# Bioinspired Citrate–Apatite Nanocrystals Doped with Divalent Transition Metal Ions

Francisco Javier Martínez-Casado,<sup>\*,†,‡</sup> Michele Iafisco,<sup>§</sup> José Manuel Delgado-López,<sup>†</sup> Carla Martínez-Benito,<sup>||</sup> Catalina Ruiz-Pérez,<sup>||</sup> Donato Colangelo,<sup>⊥</sup> Francesca Oltolina,<sup>⊥</sup> Maria Prat,<sup>⊥</sup> and Jaime Gómez-Morales<sup>\*,†</sup>

<sup>†</sup>Laboratorio de Estudios Cristalográficos, IACT (CSIC-UGR), Avda. Las Palmeras, no. 4, 18100 Armilla, Granada

<sup>‡</sup>MAX IV Laboratory, Lund University, Ole Römers väg 1, 223 63, Lund, Sweden

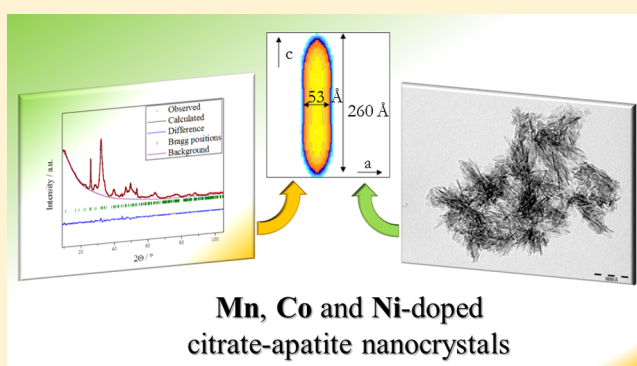
<sup>§</sup>Institute of Science and Technology for Ceramics (ISTEC), National Research Council (CNR), Via Granarolo 64, 48018 Faenza (RA), Italy

<sup>||</sup>Laboratorio de Rayos X y Materiales Moleculares (MATMOL), Departamento de Física, Facultad de Ciencias (Sección Física), Universidad de La Laguna, Tenerife, Spain

<sup>⊥</sup>Dipartimento di Scienze della Salute, Università del Piemonte Orientale, Via Solaroli, 17, 28100 Novara, Italy

## Supporting Information

**ABSTRACT:** Bioinspired citrate–carbonate–apatite (cAp) nanocrystals doped with divalent transition metal (M) ions, i.e., Mn<sup>2+</sup>, Co<sup>2+</sup>, and Ni<sup>2+</sup>, were prepared by batch thermal decomplexing of Ca<sup>2+</sup>/M/citrate/phosphate/carbonate solutions at 80 and 37 °C, with initial Ca<sup>2+</sup>/M molar ratios of 9:1 and 5:5, and at different crystallization times ranging from 1 to 96 h. A thorough chemical, crystallographic, and morphological characterization was carried out on the doped nanocrystals revealing that (i) using similar crystallization conditions the amount of incorporated M normally followed the order Mn<sup>2+</sup> > Co<sup>2+</sup> > Ni<sup>2+</sup>; (ii) the growth of nanocrystals was clearly enhanced at 80 °C and when a lower amount of M was incorporated in the crystal structure; (iii) the increase of the M content increased the aspect ratio (length/width) of the M-doped cAp nanocrystals compared to undoped ones, (iv) the incorporation of the 6.5 wt % of M is a threshold for the long-range order of the nanocrystal; in fact, with a higher M content, amorphous materials were mainly produced. Additionally, we found that citrate controlled the activity of hydrated M ions in solution, the extension of the doping process, and protected the M ions against oxidation in solution as well as in the outermost layer of doped nanocrystals. Preliminary in vitro cytotoxicity studies on the murine MS1 endothelial cell line showed that the produced Mn<sup>2+</sup>- and Co<sup>2+</sup>-doped nanocrystals were highly biocompatible at doses comparable to those of undoped ones, with the exception of the nanocrystals substituted with the highest Co<sup>2+</sup> content at the higher doses.



Mn, Co and Ni-doped  
citrate-apatite nanocrystals

## 1. INTRODUCTION

Apatite (Ap) nanocrystals are widely used in orthopedics, dentistry, and more recently also for other exciting nanotechnological applications as drug nanocarriers, nanocatalysts, and fertilizers due to their well-known properties of biocompatibility, biodegradability, osteoinductivity, and ability to link a wide range of molecules to a high extent.<sup>1–4</sup> In addition, it is well reported that Ap nanocrystals having features very close to those present in bone in terms of size, chemical composition, and morphology, the so-called “biomimetic” Ap, display enhanced biological and technological performances.<sup>5–7</sup> Therefore, many synthetic methodologies to prepare “biomimetic” Ap nanocrystals have been developed in the last few years,<sup>1,8–10</sup> and in most of them organic templates or additives were used to finely control nucleation and crystal growth.<sup>10–12</sup>

Recently Delgado-López et al. prepared bioinspired citrate–carbonate–apatite (cAp) nanocrystals having mean lengths ranging from 20 to 100 nm by batch thermal decomplexing of calcium/citrate/phosphate/carbonate solutions.<sup>13</sup> Citrate was employed as an organic additive during the Ap synthesis because it was found that it is strongly bound to bone Ap surface, and it accounts for about 5.5 wt % of the total organic component of bone tissue.<sup>14</sup> The presence of citrate in the reaction environment enables the formation of homogeneous metastable solutions at pH > 8.3, avoiding the instantaneous nucleation of calcium carbonate or calcium phosphate.<sup>13,15</sup> At the same time, the increase of the temperature produces a

Received: July 22, 2015

Revised: October 2, 2015

Published: November 11, 2015

gradual and homogeneous release of  $\text{Ca}^{2+}$  ions leading to the formation of amorphous calcium phosphate (ACP) that transforms to nanocrystalline carbonate apatite platelets with citrate adsorbed on the surface.<sup>16</sup> Citrate plays the dual role of driving a growth pathway via an amorphous precursor and controlling the size of the nanocrystals by the nonclassical oriented aggregation mechanism.<sup>17</sup> Moreover, cAp nanocrystals display excellent biocompatibility properties in cell biological systems,<sup>13</sup> and it was demonstrated that they can be used as pH-responsive delivery system of the anticancer drug doxorubicin inside cells.<sup>18</sup>

Ap nanocrystals doped with foreign ions have also recently attracted remarkable attention, since the ionic substitution is a powerful tool to improve their performances for different applications.<sup>19</sup> Substitution of doping ions (i.e., cations and anions) in the Ap crystal lattice can commonly occur. Indeed, bone Ap nanocrystals are substituted with several foreign ions such as  $\text{CO}_3^{2-}$ ,  $\text{HPO}_4^{2-}$ ,  $\text{SiO}_4^{4-}$ ,  $\text{Na}^+$ ,  $\text{Mg}^{2+}$ ,  $\text{Mn}^{2+}$ , and other minor elements.<sup>1</sup> Because of its high flexible structure, Ap can host monovalent, divalent, and even trivalent cations, as well as simple monovalent anions or oxoanions.<sup>19,20</sup>

The aim of this work is the preparation and characterization of bioinspired cAp nanocrystals doped with different functional metal (M) ions by the method of thermal decomplexing of calcium/M/citrate/phosphate/carbonate metastable solutions.<sup>13,15–17</sup> Three divalent M cations, such as  $\text{Mn}^{2+}$ ,  $\text{Co}^{2+}$  and  $\text{Ni}^{2+}$ , were selected as doping ions to modify the crystal structure of the nanocrystals and to improve their features for novel or better biological and technological applications.

$\text{Mn}^{2+}$  ion plays an important role in bone metabolism since it influences regulation of bone remodeling, and its deficit causes reduction of organic matrix synthesis and retards endochondral osteogenesis.<sup>21</sup>  $\text{Mn}^{2+}$ -doped carbonate-Ap nanocrystals promote human osteoblasts proliferation, activation of their metabolism and thereby bone growth.<sup>22</sup> The presence of  $\text{Mn}^{2+}$  in the crystalline structure of Ap was also found to positively influence the adhesion of bone cells to an implant material, their spread and viability.<sup>23</sup> In view of this, the  $\text{Mn}^{2+}$  ion can be considered as an optimal agent to improve the osteoconductivity and osteointegration of cAp-based materials for bone tissue engineering.

$\text{Co}^{2+}$  ion is well reported as an antibacterial and antiviral agent in various organic complexes.<sup>24</sup> Nanocrystalline Ap doped with  $\text{Co}^{2+}$  presents antibacterial activity against different strains, i.e., *Staphylococcus aureus*, *Micrococcus luteus*, and *Shigella flexneri*.<sup>20</sup> Moreover Ap enriched with a large content of  $\text{Co}^{2+}$  ions was found to display a highly beneficial effect for osteoporotic bone tissue regeneration.<sup>25</sup> As a result,  $\text{Co}^{2+}$  can be effective to provide antimicrobial and antibacterial properties to cAp nanocrystals with the final aim to manufacture multifunctional materials for bone and dental applications.

Furthest from the biomedical field,  $\text{Ni}^{2+}$  is one of the most active M ions able to catalyze many interesting reactions,<sup>26,27</sup> and also Ap has been reported as a recyclable low-cost material to support catalysts for organic synthesis.<sup>28</sup> Recently,  $\text{Ni}^{2+}$ -substituted Ap has revealed good catalytic activity in the process of methane dry reforming.<sup>29</sup> Therefore, the addition of  $\text{Ni}^{2+}$  ions in the cAp structure can be useful to prepare non-hazardous and biodegradable “green” material as a heterogeneous nanocatalyst.

In this work, the physical–chemical and crystallographic properties of the prepared M-doped cAp nanocrystals have been thoroughly characterized to assess the influence of the

selected ions on the chemical and structural properties of the cAp. Moreover, the biocompatibility of  $\text{Mn}^{2+}$ - and  $\text{Co}^{2+}$ -doped nanocrystals has been characterized in the murine MS1 endothelial cell line to evaluate their possible use for biomedical applications.

## 2. MATERIALS AND METHODS

**2.1. Reagents.** Calcium chloride dihydrate ( $\text{CaCl}_2 \cdot 2\text{H}_2\text{O}$ , Bioxtra,  $\geq 99.0\%$  pure), nickel chloride hexahydrate ( $\text{NiCl}_2 \cdot 6\text{H}_2\text{O}$ , ACS reagent, purity = 99.999%), manganese chloride tetrahydrate ( $\text{MnCl}_2 \cdot 4\text{H}_2\text{O}$ , ACS reagent, purity), cobalt chloride hexahydrate (reagent grade), sodium citrate tribasic dihydrate ( $\text{Na}_3(\text{Cit}) \cdot 2\text{H}_2\text{O}$  where Cit = citrate =  $\text{C}_6\text{H}_5\text{O}_7$ , ACS reagent,  $\geq 99.0\%$  pure), sodium phosphate dibasic ( $\text{Na}_2\text{HPO}_4$ , ACS reagent,  $\geq 99.0\%$  pure) and sodium carbonate monohydrate ( $\text{Na}_2\text{CO}_3 \cdot \text{H}_2\text{O}$ , ACS reagent, 99.5% pure), and hydrochloric acid (HCl, ACS reagent, 37 wt % in  $\text{H}_2\text{O}$ ) were provided by Sigma-Aldrich. All solutions were prepared with ultrapure water (0.22  $\mu\text{S}$ , 25 °C, Milli-Q, Millipore).

**2.2. Crystallization Methods.** The experiments were carried out by thermal treatment of metastable solutions containing  $\text{Ca}^{2+}$ /M-citrate complexes in the presence of phosphate and carbonate ions, at pH = 8.5 (where M is  $\text{Mn}^{2+}$ ,  $\text{Co}^{2+}$ , or  $\text{Ni}^{2+}$ ). Materials were synthesized on the basis of the procedure reported elsewhere.<sup>13</sup> Briefly, two solutions of (a)  $x \text{CaCl}_2 + y \text{MCl}_2$  ( $x = 0.09$  or  $0.05 \text{ M}$  and  $y = 0.01$  or  $0.05 \text{ M}$ , to get 9:1 and 5:5 molar ratios, respectively) +  $0.4 \text{ M Na}_3(\text{Cit})$  and (b)  $0.12 \text{ M Na}_2\text{HPO}_4 + 0.2 \text{ M Na}_2\text{CO}_3$  were mixed (1:1 v/v, 200 mL total) at 4 °C, and the pH was adjusted to 8.5 with diluted HCl. The undoped sample (cAp) was obtained using a  $0.10 \text{ M CaCl}_2$  M-free solution in the aforementioned procedure. The mixed solution was introduced in a 250 mL round-bottom flask, sealed with a glass stopper and, without delay, immersed in a water bath at 80 °C. A set of experiments using an initial 9:1 Ca/M ratio was also carried out at 37 °C to assess the influence of the temperature. The crystallization experiments were stopped at different maturation times ranging from 1 to 96 h. Once finished, the precipitates were subjected to three consecutive cycles of washing by centrifugation with ultrapure water. Afterward they were freeze-dried overnight at  $-50$  °C under a vacuum (3 mbar).

**2.3. Characterization Methods.** The study of the speciation of  $\text{Ca}^{2+}$ -citrate and M-citrate aqueous solutions as a function of the temperature was carried out to assess the stability of these complexes in solution prior the crystal precipitation and to correlate their activities with the amount of metal incorporated in the crystalline structure of the precipitates. Calculations were performed with Phreeqc speciation software<sup>30</sup> with the minteq v4.dat database using the initial Ca/M ratio 9:1 at pH 8.5. The aqueous species considered in the calculations are shown in Supporting Information.

The M, Na, Ca, and P contents were determined by inductively coupled plasma-optical emission spectrometry (ICP-OES) using a PerkinElmer Optima 8300 spectrometer. Samples were dissolved in 1 wt % ultrapure nitric acid and analyzed in triplicate. The crystallographic characterization and the microstructural analysis (average crystal size and shape) were carried out by powder X-ray diffraction (PXRD). PXRD patterns were collected in reflection mode (on a Si flat sample holder), using a Cu  $K\alpha$  radiation ( $K\alpha_2/K\alpha_1 = 0.476$ ) on a PANalytical X'Pert PRO MPD diffractometer equipped with a PIXcel RTMS detector operating at 45 kV and 40 mA. For the incident beam, fixed anticatter and divergence slits of  $1^\circ$  and  $0.5^\circ$ , respectively, were used. The  $2\theta$  range varied from  $5^\circ$  to  $104^\circ$  with a step size of ( $2\theta$ )  $0.013^\circ$ . The Rietveld refinement of collected X-ray diffraction (XRD) data was accomplished by using the Fullprof software package.<sup>31</sup> Transmission electron microscopy (TEM) observations as well as selected area electron diffraction (SAED) and energy-dispersive X-ray spectroscopy (EDS) analysis were performed with a STEM Philips CM 20 microscope operating at 80 kV. The powder samples were ultrasonically dispersed in ethanol (absolute,  $\geq 99.8\%$ ), and then a few droplets of the slurry were deposited on conventional copper microgrids prior to observation. The analysis of the electrophoretic mobility ( $\zeta$ -potential) of samples was performed in a Zetasizer Nano

analyzer (Malvern, UK) using disposable folded capillary cells at 25 °C. Samples were prepared by suspending particles in deionized water with pH  $\sim$  6.5.

**2.4. Cytotoxicity Tests.** The murine MS1 endothelial cell line was maintained in Dulbecco's modified Eagle's medium (DMEM), 10% fetal calf serum, 50 U/mL penicillin, and 50  $\mu$ g of streptomycin (complete medium), by transplanting them twice a week. For toxicity tests, cells were incubated ( $10 \times 10^3/0.4$  cm<sup>2</sup> microwell) for 24 h; then different concentrations of M-doped and control undoped nanoparticles were added in 100  $\mu$ L of complete medium. Soluble doxorubicin hydrochloride (DOXO, C<sub>27</sub>H<sub>29</sub>NO<sub>11</sub>HCl, 98.0–102.0% HPLC grade) was used as a control toxic reagent. After 2–3 days incubation, cells viability was evaluated by the 3-(4,5-dimethylthiazol-2-yl)-2,5-diphenyltetrazolium bromide (MTT) colorimetric assay. Briefly, 20  $\mu$ L of MTT solution (5 mg mL<sup>-1</sup> in a PBS solution) was added to each well. The plate was then incubated at 37 °C for 3 h, and then the supernatants were carefully aspirated. Afterward, 125  $\mu$ L of 0.2 M HCl isopropanol was added to dissolve formazan crystals. A 100  $\mu$ L aliquot was then removed carefully, and the optical density was measured in a multiwell reader (2030 Multilabel Reader Victor TM X4, PerkinElmer) at 570 nm. Viability of parallel cultures of untreated cells was taken as 100% viability, and values obtained from cells undergoing the different treatments were referred to this value. Experiments were performed four times using three replicates for each sample.

**2.5. Statistical Analysis.** Experiments were carried out in triplicate, and data are expressed as mean  $\pm$  standard error. Statistical analyses were performed using independent *t* tests for two groups comparisons and a one-way analysis of variance (ANOVA), after checking homogeneity of variance using Levene's test, in the case of multiple comparisons. ANOVA was followed by postdoc Scheffé's test. Differences at *p* < 0.05 were considered to be statistically significant.

### 3. RESULTS

#### 3.1. Thermal Destabilization of Metal-Citrate Complexes and Metal Substitution in the cAp Nanocrystals.

Figure 1 shows the evolution of the calculated ionic activities of M-citrate complexes and the free solvated M cations as a function of temperature. Ca(citrate)<sup>-</sup> revealed higher activity than Co(citrate)<sup>-</sup>, Mn(citrate)<sup>-</sup>, and Ni(citrate)<sub>2</sub><sup>4-</sup>, respectively. Similarly, free Ca<sup>2+</sup> displayed higher activity in comparison to the other free solvated ions (i.e., Mn<sup>2+</sup>, Co<sup>2+</sup>, and Ni<sup>2+</sup>). The fact that the activities of all M-citrate complexes

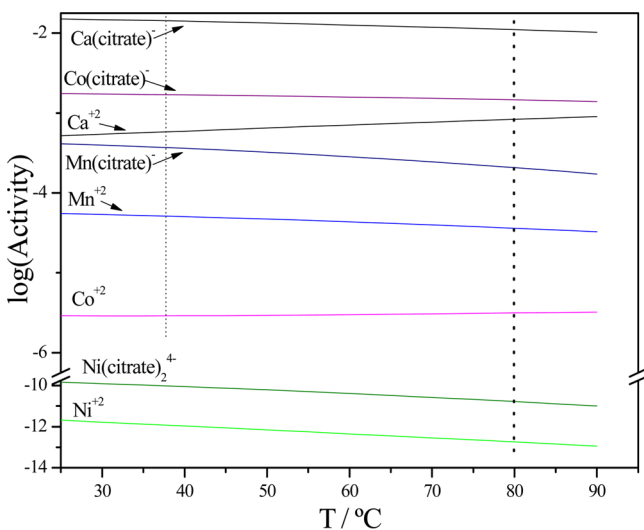


**Figure 1.** Calculated ionic activities of Ca(citrate)<sup>-</sup>, M-citrate complexes, and the free solvated cations as a function of the temperature, for the (9:1) initial Ca/M molar ratio.

decrease as a function of the temperature, because of their thermal destabilization, validates the application of the thermal decomplexing method for precipitating M-doped apatites in the presence of citrate.

On the basis of these data, only in the case of Ni<sup>2+</sup>, whose activity was very low, the Ca<sup>2+</sup> ions within the apatite structure could be replaced with a low efficiency. The calculations also suggest that the different stability of the M-citrate complexes and their evolution with the temperature can be a key factor influencing the doping of the apatitic structure.

The M content of the doped nanocrystals is shown in Figure 2, for (9:1) initial Ca/M molar ratio at 80 °C, and in Figure S1

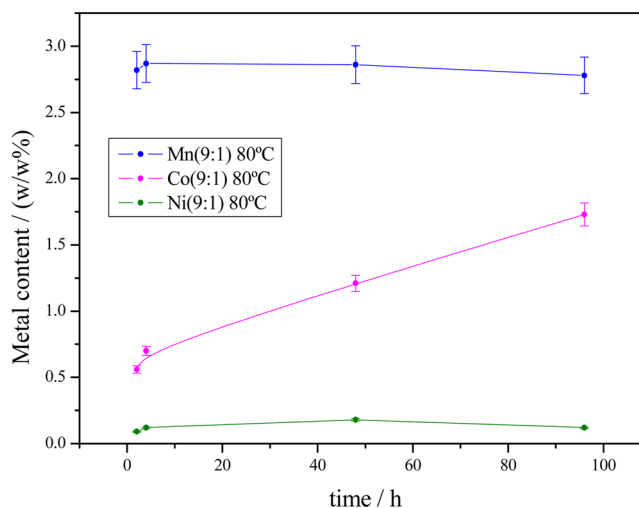


**Figure 2.** Transition metal content (w/w%) as a function of maturation time in the M-doped cAp nanoparticles prepared at 80 °C with an initial Ca/M ratio of 9:1.

for samples prepared in the rest of studied conditions. At 80 and 37 °C the higher M content was found in samples prepared in the presence of Mn<sup>2+</sup>, rather than in those precipitated in the presence of Co<sup>2+</sup> and Ni<sup>2+</sup>, in agreement with the order in which the activities of these ions decreased in solution. At 80 °C, the Ca/M ratio 5:5 significantly favored the incorporation of M irrespective of its nature, and, in this regard, it is worth noting that in some samples the Mn<sup>2+</sup> content was almost twice of that of Ca<sup>2+</sup> (Table S1, Supporting Information).

In the cases of Mn<sup>2+</sup> and Co<sup>2+</sup> the doping process is controlled by the thermal evolution of the ionic activities in solution, which are temperature-dependent. In fact, Mn-doped cAp crystals showed less Mn<sup>2+</sup> content at 80 °C than at 37 °C in agreement with the decrease of Mn<sup>2+</sup> activity with temperature. In contrast, Co-doped crystals showed a higher Co<sup>2+</sup> content at the highest temperature, since the activity of free Co<sup>2+</sup> increased with temperature. Differently, the amount of Ni<sup>2+</sup> inside the apatitic structure did not follow a trend as a function of temperature because of its very low activity in solution. The time evolution of M content shows that Mn<sup>2+</sup> and Ni<sup>2+</sup> are incorporated during the first 4 h of reaction, and then the content of these elements remains almost constant (Figure 2). Only in the case of Co<sup>2+</sup> a linear increase in the amount of M incorporated as a function of time has been found.

The full elemental composition including the weight percentage of Ca, P, and Na, and the (Ca+M)/P and Ca/M molar ratios, is shown in Table S1 of Supporting Information.

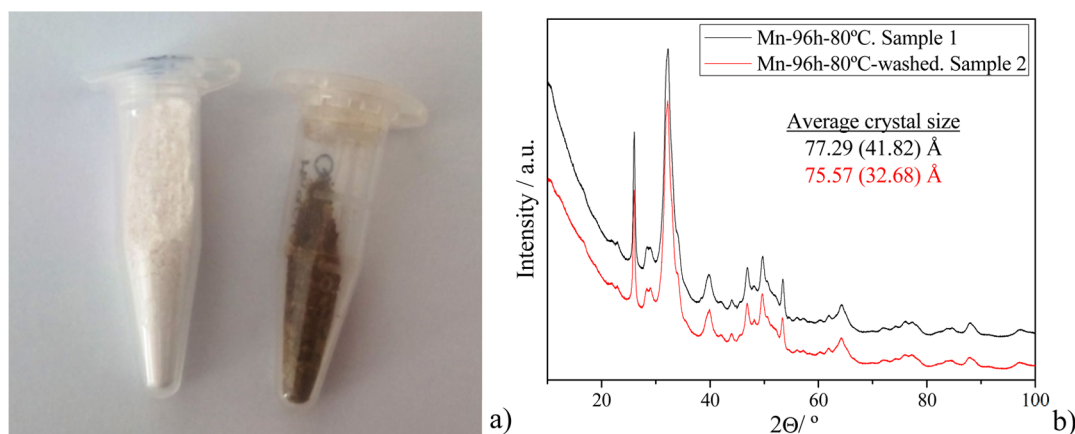


**Figure 3.** (a) Picture showing the effect of the metal oxidation when removing the citrate coating in a Mn-doped cAp sample (Mn(9:1)-96h-80 °C): samples before (white powder) and after washing (brown powder) with 0.1 M NaOH solution; (b) XRD diagrams of the samples before and after washing with 0.1 M NaOH.

The (Ca+M)/P molar ratio of all the studied samples did not significantly vary as a function of maturation time revealing only slight changes in the structural composition of M-doped cAp nanocrystals. Conversely, the Ca/M molar ratio was significantly affected by the different M content that is able to enter and substitute for  $\text{Ca}^{2+}$  ions in the apatitic structure.

It was already reported that cAp nanocrystals obtained by the thermal decomplexing technique are covered by adsorbed citrate and counterions.<sup>14</sup> Herein we show that this layer (composed of citrate and  $\text{Na}^+$ ) can be removed by washing the crystals in a basic solution (NaOH 0.1 M). In fact, FTIR spectroscopy revealed that the characteristic asymmetric stretching mode of  $-\text{COO}^-$  groups of citrate ions at  $1595\text{ cm}^{-1}$ ,<sup>15</sup> practically disappears after this treatment (Figure S2 of Supporting Information). FTIR spectra of M-doped cAp nanoparticles (Figure S2) also showed the main broad band at  $\sim 1030\text{ cm}^{-1}$  with a shoulder at around  $1074\text{ cm}^{-1}$  corresponding to the asymmetric stretching mode of  $\text{PO}_4^{3-}$  groups and the bands at  $\sim 962\text{ cm}^{-1}$  and  $\sim 603\text{ cm}^{-1}$  ascribed to the symmetric stretching and bending mode of  $\text{PO}_4$  groups, respectively. The presence of  $\text{CO}_3^{2-}$  bands at  $\sim 1465\text{ cm}^{-1}$  and  $\sim 880\text{ cm}^{-1}$  (shoulder) indicated that  $\text{CO}_3^{2-}$  ions replaced the  $-\text{OH}$  groups (A-type carbonation).<sup>13</sup> The absence of bands at  $3567$  and  $631\text{ cm}^{-1}$  corresponding to the stretching and librational modes of OH groups confirmed the A-type carbonate substitutions. Additionally the presence of the bands at  $1415$  and  $873\text{ cm}^{-1}$  proved also the existence of B-type carbonate substitutions ( $\text{CO}_3^{2-}$  replacing  $\text{PO}_4^{3-}$  groups).

The elemental analysis (Table S1, Supporting Information) revealed that the  $\text{Na}^+$  content in the washed samples decreased significantly with respect to the unwashed precipitates indicating that the major part of  $\text{Na}^+$  was entrapped in the surface layer. On the contrary, the M content remained almost unaltered when the citrate layer was removed, proving that most of M was incorporated into the apatite structure. An additional result found in the washed samples was that the  $\text{Na}^+$  content was similar regardless of the nature of the transition metal (Mn or Co) and the initial Ca/M ratio (see Table S2 of Supporting Information). The amount of  $\text{Na}^+$  and M in the analyzed samples suggests that the metal composition for the M-doped nanoparticles can be represented by the general chemical formula:  $\text{Ca}_{5-x-y}\text{Na}_{2x}\text{M}_y$ .

Interestingly, the formation of M-citrate complexes in solution prevents the oxidation of  $\text{Mn}^{2+}$  at basic pH, and,

moreover, the citrate coating around the crystals avoids metal oxidation of the doped nanocrystals. In fact, after removing the citrate coating with 0.1 M NaOH a change of color from white to brown occurred, indicating the oxidation from  $\text{Mn}^{2+}$  to  $\text{Mn}^{3+/4+}$  (Figure 3a). The structure and sizes of the doped apatites, however, remained unaltered after this treatment since the XRD patterns of the as-synthesized and washed samples were similar (Figure 3b). This fact indicates that oxidation of manganese took place at the outermost layer of the doped nanocrystals.

### 3.2. Microstructure of M-Doped cAp Nanocrystals.

The XRD diagrams of the samples prepared at the different conditions (Figure S3, Supporting Information) showed the diffraction peaks of hydroxyapatite single phase. Concerning the interpretation of our experimental XRD patterns, we adopted the hexagonal symmetry for this phase, according to (JCPDS 9-432), for the sake of practice and simplicity. Thus, the characteristics reflections appear at  $2\theta$   $25.87^\circ$  (plane 00.2), the broad peak due to the triplet at  $31.77^\circ$ ,  $32.19^\circ$ , and  $32.90^\circ$ , which correspond to planes 21.1, 11.2, and 30.0 and other main peaks at  $39.81^\circ$ ,  $46.71^\circ$ ,  $49.46^\circ$ , and  $53.14^\circ$ , which correspond to the planes 31.0, 22.2, 21.3, and 00.4 respectively.<sup>32</sup>

The Rietveld refinements were performed using the *FullProf* program.<sup>31</sup> The unit cell parameters, obtained from the most crystalline samples by DICVOL04,<sup>33</sup> belong to the hexagonal system, space group  $P6_3/m$ , and they were the same as those reported for hydroxyapatite. The refinements started from the atomic positions reported by Wilson et al.<sup>34</sup> (in which structure the carbonate groups are included), constraining the composition of transition M and Ca according to the M content calculated by ICP-OES. The peak profiles were described by a Thompson–Cox–Hastings (TCH) pseudo-Voigt profile function, whereas a Chebyshev polynomial was used for the background description.

The parameters that were systematically refined included the unit cell ( $a$  and  $c$ ; 2), preferred orientation (1), size and shape (anisotropic Lorentzian size broadening by spherical harmonics in the Laue class  $6/m; 3$ ), isotropic strain (1), background (15), and overall B-factor (1). The refinements presented great robustness and repeatability for all samples (see Figure 4 showing the fitting for two of the samples: Mn(9:1)-Ap-2h-80 °C and Co(9:1)-Ap-48h-80 °C).

The microstructural analysis provided the average crystallite size, i.e., the mean size of the diffractive crystal domains

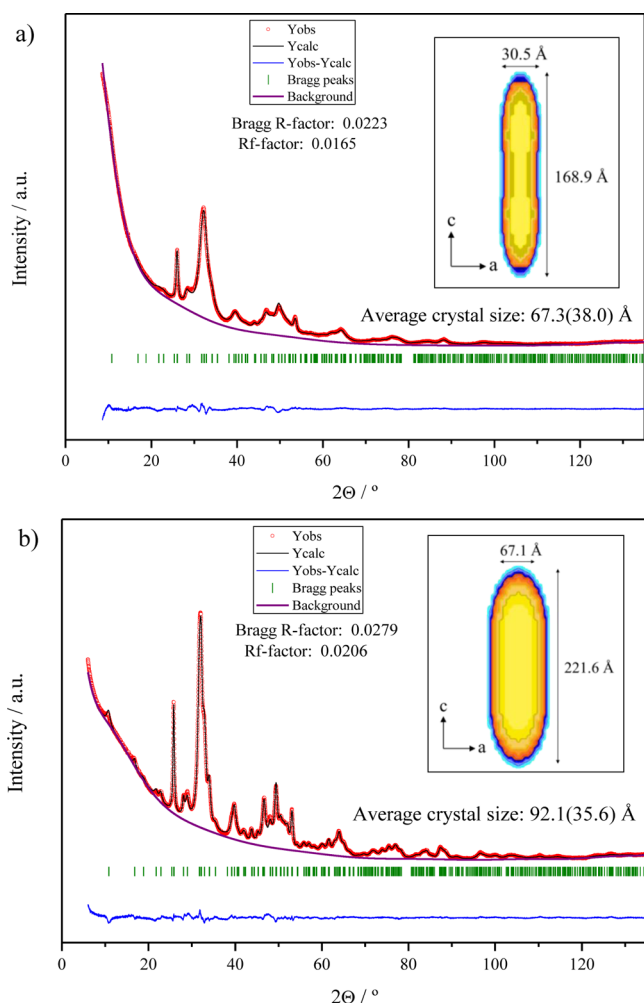


**Figure 4.** Examples of Rietveld refinements of the samples (a) Mn(9:1)-Ap-2h-80 °C and (b) Co(9:1)-Ap-48h-80 °C, showing the excellent agreement between the observed and calculated diffraction patterns. The average crystallite size (isotropic), the calculated sizes ( $D_{001}$  and  $D_{hk0}$ ), and the shape of the crystalline domains are shown in the inset.

(referred to the volume of these domains). The standard deviation in those values corresponds to the anisotropy of the crystal domains, since anisotropic size broadening corrections were applied.

The average crystallite sizes for the different samples are reported in Table 1. The largest crystallites were found for cAp, and then the average sizes decreased gradually from Ni-, Co-, and Mn-doped samples. Temperature and Ca/M ratio affected significantly the crystallite sizes. In fact, the samples prepared at

**Table 1.** Average crystallite size (Å) and relative standard deviation (as Anisotropy, in parentheses), of cAp and M-doped cAp nanocrystals synthesized at 80 °C using the initial Ca/M molar ratio of 9:1

time/h	cAp	Mn-cAp	Co-cAp	Ni-cAp
1	68.8(39.9)	35.9(22.3)	52.5(66.1)	43.6(21.3)
2	67.3(38.0)	45.6(26.8)	61.9(36.0)	64.8(30.6)
4	70.8(39.4)	47.5(25.6)	66.3(35.3)	71.6(31.9)
48	110.6(36.6)	66.2(35.1)	92.1(35.6)	106.5(40.6)
96	127.1(46.6)	77.3(41.8)	97.7(39.1)	118.7(48.0)

37 °C showed lower values than those obtained at 80 °C. Similarly, samples prepared with the Ca/M ratio of 5:5 were smaller than those prepared with the Ca/M ratio of 9:1.

The dimensions of the crystal domains were estimated also in the different directions of the crystals, besides the average crystallite size. The cAp crystals, with a hexagonal unit cell (Laue group  $6/m$ ), show two main dimensions,  $D_{001}$  and  $D_{hk0}$ , that are the longest and the shortest, respectively. The average size of crystal domains reported in Table 2 are related to the samples prepared at 80 °C using a Ca/M initial ratio of 9:1 (see Table S3 in Supporting Information for data relative to the other M-doped cAp nanocrystals).

The values of  $D_{001}$  are clearly higher than those of  $D_{hk0}$  indicating that the crystal domains were elongated along the  $c$ -axis.

### 3.3. Crystal Growth of M-Doped cAp Nanocrystals.

The growth behavior of the nanocrystals as a function of time is shown in Table 1 and in Figure S4 of the Supporting Information. Crystal growth is faster during the first crystallization stages, whereas growth cessation is observed at the longer times of each run.

The growth of nanocrystals is clearly enhanced when temperature increased and the M content decreased, Ni-doped cAp nanocrystals showing the highest growth while those doped with Co and Mn the lowest. In the absence of M, i.e., undoped cAp, the growth is even faster. Thus, the doping process directly affected the final size and shape of the nanocrystals in the sense that a lower M content yielded longer and wider crystals. The plot of the average crystallite size versus the percentage of M content for crystallization times of 2, 4, 48, and 96 h graphically reports this trend (Figure 5). Interestingly, a crystal size of around 20 Å (2–3 unit cells) was found above 6.5% of M content, in all the cases. This size can be considered the frontier between crystalline and amorphous structures.

On the other hand, we found that the higher the M content the more difficult the growth is in the (10.0) and equivalent planes of cAp nanocrystals. The reason is likely due to the stronger (shorter) bond of the citrate molecules with M than with Ca in the outermost apatite layer, i.e.,  $d(\text{Ca(II)}-\text{O}) \approx 2.4$  Å;  $d(\text{Mn(II)}-\text{O}) \approx 2.2$  Å;  $d(\text{Co(II)}-\text{O}) \approx 2.1$  Å;  $d(\text{Ni(II)}-\text{O}) \approx 2.1$  Å. In a thorough study about the Co-doped hydroxyapatite particles produced in the absence of carboxylated molecules by Veselinovic et al.,<sup>35</sup> the authors showed that samples with higher  $\text{Co}^{2+}$  content display not only smaller sizes but also lower aspect ratio than undoped particles. In agreement with these results, herein we prove that citrate plays a decisive role in shaping the M-doped nanocrystals, avoiding the growth in the (hk.0) planes and yielding nanoparticles with greater aspect ratios.

Another interesting result of the microstructural study is that the volume of the unit cell varies between different samples and decreases with crystallization time (Figure 6a). This can be explained by the crystal size, which, in fact, presents an indirect relationship with the unit cell volume: the smaller the crystals, the bigger the cell volume (Figure 6b). In all cases the variation of the unit cell is more pronounced in the  $a$  than in the  $c$  parameter (Table S4, Supporting Information). This suggests that the citrate anions bind more strongly to the outermost (hk.0) planes as the transition M content increases, and then, the few unit cells in the nanocrystals are more deformed than in the bulk of bigger crystals. In fact, the strain is bigger in smaller crystals, and therefore, in crystals that were precipitated at shorter reaction times (Figure S6, Supporting Information).

**Table 2.** Average size ( $D$ ) of crystal domains along the  $[00l]$  and  $[hk.0]$  directions of cAp and M-doped cAp nanocrystals synthesized at 80 °C using the initial Ca/M molar ratio of 9:1

time/h	cAp			Mn-Ap			Co-Ap			Ni-Ap		
	$D_{00l}/\text{\AA}$	$D_{hk.0}/\text{\AA}$	$D_{00l}/D_{hk.0}$	$D_{00l}/\text{\AA}$	$D_{hk.0}/\text{\AA}$	$D_{00l}/D_{hk.0}$	$D_{00l}/\text{\AA}$	$D_{hk.0}/\text{\AA}$	$D_{00l}/D_{hk.0}$	$D_{00l}/\text{\AA}$	$D_{hk.0}/\text{\AA}$	$D_{00l}/D_{hk.0}$
1	254.63	46.63	5.5	128.52	25.25	5.1	202.29	34.55	5.9	124.25	31.94	3.9
2	231.14	44.07	5.2	168.9	30.5	5.5	220.8	40.7	5.4	188.2	45.2	4.2
4	241.13	46.48	5.2	161.7	32.6	5.0	213.1	44.2	4.8	193.8	50.1	3.9
48	229.46	81.79	2.8	218.8	45.3	4.8	221.6	67.1	3.3	257.1	78.6	3.3
96	305.26	94.73	3.2	260.2	52.7	4.9	251.6	70.5	3.6	289.6	84.3	3.4

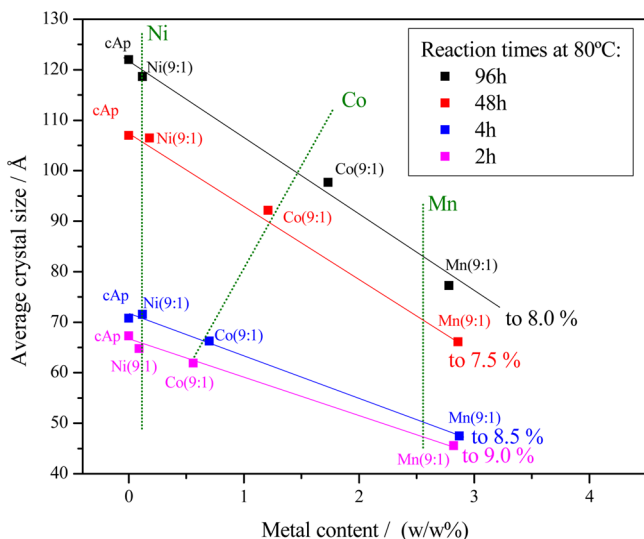


**Figure 5.** Average crystallite size versus M content of the cAp and the M-doped cAp nanocrystals synthesized at different times and at 80 °C using the initial Ca/M molar ratio of 9:1.

**3.4. Size and Shape Distribution by TEM.** TEM analyses were carried out on the samples prepared with the longest crystallization time (96 h). The mean length ( $L$ ) along the longest axis, the mean width ( $W$ ), and the mean aspect ratio ( $R$ , ratio between  $L$  and  $W$ ) were determined from TEM micrographs of samples precipitated with Ca/M ratio 9:1 using 40–50 particles in each micrograph (Figure 7a–c).

The  $L$  and  $W$  values of the nanocrystals (which correspond to the dimensions in the  $[00l]$  and  $[hk.0]$  directions, respectively) decreased gradually from the undoped cAp to Ni-, Co-, and Mn-doped cAp nanoparticles (in this order), showing a correlation with the content of transition M (Table 3). It is worth noting that  $W$  values are strongly affected by the presence of transition M in the cAp structure. The values of the aspect ratio  $R$ , which correspond to the anisotropy in the shape of the crystals, increased in the opposite order, so the higher the M content the more pronounced the anisotropy is, yielding more elongated morphologies. This can be clearly observed, for example, when comparing Mn- and Ni-doped nanoparticles (Figure 7a,c).

The results for the average sizes and shapes obtained from TEM observations were in rather good agreement with the average crystallite sizes calculated by microstructural analysis (Table 3), suggesting that individual particles correspond to single crystals. On the other hand, samples with a higher M content show much smaller sizes, and the particles appear agglomerated, so their size could not be estimated, as is the case of the Mn(5:5) sample (Figure S5 of Supporting Information).

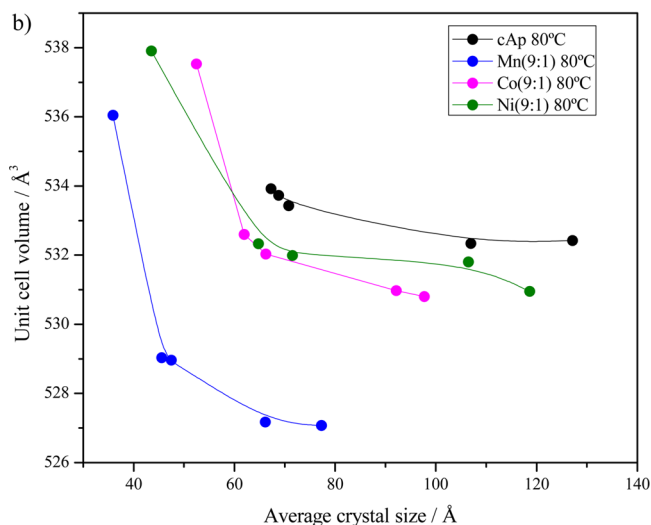
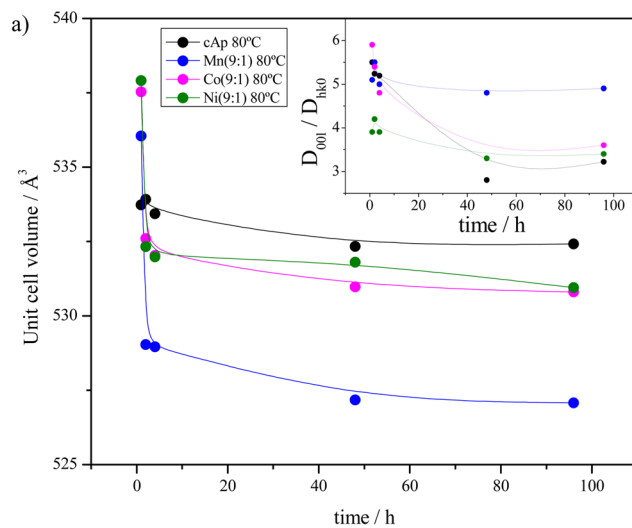


**Figure 6.** (a) Unit cell volume and  $D_{00l}/D_{hk.0}$  ( $= L/W$ ) ratio (in the inset) as a function of the reaction time and (b) unit cell volume versus average crystal size of the undoped cAp and the M-doped cAp nanocrystals synthesized at 80 °C using the initial Ca/M molar ratio of 9:1. The lines are simply included to show the tendencies.

**3.5.  $\zeta$ -Potential of M-Doped cAp Suspensions.** cAp suspensions showed the most negative  $\zeta$ -potential ( $-51.4$  mV) followed by the suspensions of Mn- and Ni-doped cAp nanocrystals, whose values were  $-21.7$  and  $-19.9$  mV respectively. This finding indicated a decrease of the colloidal stability when cAp was doped with transition metals. A higher  $\zeta$ -potential of  $-6.9$  mV was measured in Co-doped cAp, indicating that this was the less stable suspension.

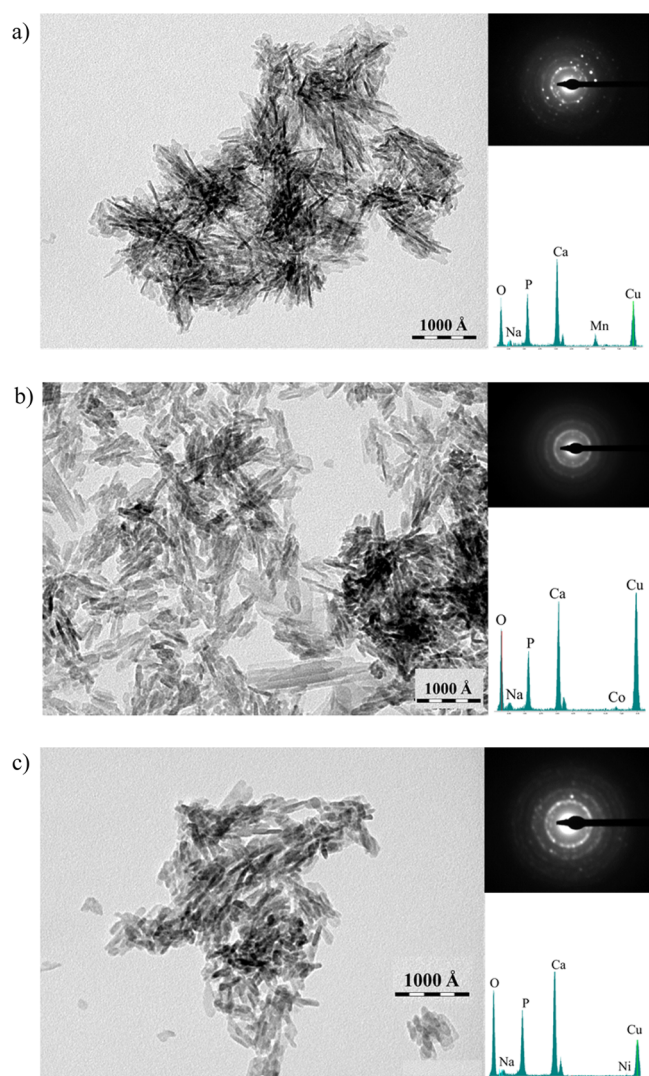


**Figure 7.** TEM micrographs of doped-Ap crystallized after 96 h: (a) Mn (9:1); (b) Co (9:1); and (c) Ni (9:1). Insets show the SAED pattern and the point analysis collected for each sample.

**3.6. Cytotoxicity of M-Doped cAp Nanocrystals.** The toxicity of  $\text{Mn}^{2+}$ - and  $\text{Co}^{2+}$ -doped nanocrystals was tested in a MTT assay on murine MS1 endothelial cells, after incubation at different concentrations ranging from 100 to 0.1  $\mu\text{g}/\text{mL}$ . No significant toxicity was observed in the case of  $\text{Mn}^{2+}$ -doped nanoparticles at any nanoparticle concentration (Figure 8). Indeed their values were superimposable to the ones of naïve undoped cAps, and in all cases cell viability was always higher than 85%. In both cases, Mn-doped and undoped cAp nanoparticles, the low toxicity observed displayed a dose-

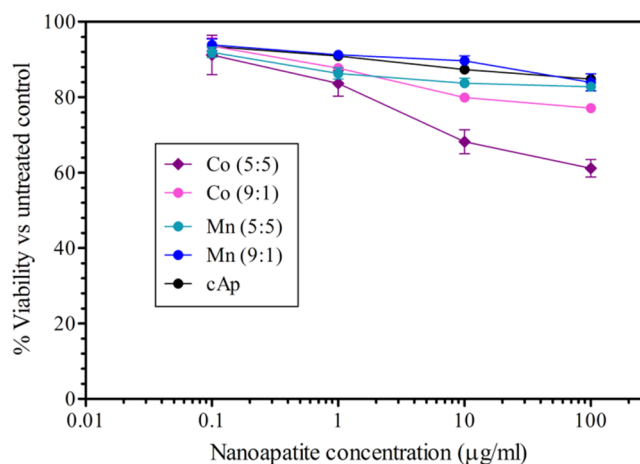


**Figure 8.** Cell viability of undoped cAp, Co-doped, and Mn-doped cAp (prepared at 80 °C, crystallization time of 96 h).

dependent relationship. Nanoparticles doped with  $\text{Co}^{2+}$  displayed a certain level of cytotoxicity, especially at the 5:5 ratio (maximum 40% at the highest concentration), but toxicity was still significantly low at the 9:1 ratio, cell survival being around 80%. Also in this case, a dose-dependent relationship was observed. Thus, since naïve undoped nanoparticles displayed already some cytotoxicity, the activity due to the doping is insignificant for Mn-doped nanoparticles and limited in the case of the Co (9:1) samples. On the other side these cells were sensitive to the toxic activity of doxorubicin, which reduced their viability to less than 40%.

#### 4. DISCUSSION

In this work the precipitation of doped cAp nanocrystals with some divalent transition metals has been carried out by thermal decomplexing of  $\text{Ca}^{2+}/\text{M}$ -citrate/phosphate/carbonate solutions. According to our data, citrate plays different roles during the doping process. First, the use of citrate as M-complexing agent enables the preparation of metastable  $\text{Ca}^{2+}/\text{M}$ /citrate/phosphate/carbonate solutions at slightly basic pH that can be easily destabilized by increasing the temperature, thus releasing the M ions and leading to the precipitation of almost monodisperse M-doped cAp nanoparticles. Second, owing to the different stability of the M-citrate complexes ( $\text{M} = \text{Mn}^{2+}$ ,  $\text{Co}^{2+}$ , and  $\text{Ni}^{2+}$ ) and its dependence with temperature, citrate controls the activity of hydrated cations in solution and therefore the extension of the doping process. Third, citrate protects the M ions against oxidation in solution as well as those present in the outermost layer of doped nanocrystals.

During the doping process M substitutes Ca positions in the cAp structure. We do not have enough data to properly assign the substitution either in Ca(I) or Ca(II) positions, since these

**Table 3.** Mean length ( $L$ ), width ( $W$ ), and aspect ratio ( $R$ ) of the cAp and the M-doped cAp nanoparticles synthesized at 80 °C using the initial Ca/M molar ratio of 9:1 and after a maturation time of 96 h<sup>a</sup>

sample	M content <sup>b</sup> / %	$L^c$ / Å	$W^c$ / Å	$R^c$ (= $L/W$ )	$D_{001}$ / Å	$D_{hko}$ / Å	$D_{001}/D_{hko}$
Mn(9:1)-96h	2.78	243 ± 93	47 ± 13	5.17 ± 0.66	260 ± 7.4	52.7 ± 0.21	4.93 ± 0.03
Co(9:1)-96h	1.73	245 ± 154	73 ± 15	3.35 ± 0.83	252 ± 3.7	70.5 ± 0.20	3.57 ± 0.02
Ni(9:1)-96h	0.12	275 ± 170	85 ± 22	3.23 ± 0.94	289 ± 4.8	84.3 ± 0.27	3.42 ± 0.02
cAp-96h		292 ± 107 <sup>d</sup>	123 ± 28 <sup>d</sup>	2.5 ± 1.0 <sup>d</sup>	305 ± 6.2	94.7 ± 0.38	3.22 ± 0.03

<sup>a</sup>Average size ( $D$ ) of crystal domains along the  $[00.l]$  and  $[hk.0]$  directions calculated from the microstructural analysis (XRD). <sup>b</sup>Transition metal content (w/w). <sup>c</sup>Measured from TEM micrographs. <sup>d</sup>Values from ref 13.

two positions are not equivalent. Site Ca(I) is smaller in volume than site Ca(II). As the ionic radii of  $\text{Mn}^{2+}$  (0.080 nm),  $\text{Co}^{2+}$  (0.0745 nm), and  $\text{Ni}^{2+}$  (0.069 nm) are lower than ionic radius of calcium of site (I) (0.099 nm), by simple reasoning one can consider that Ca(I) positions are the preferred substitution site. Nevertheless, M substitution in one or another position or in both depends not only on the ionic radii but also on the number (concentration) of doping M ions and the type and amount of anions (as in this case  $\text{CO}_3^{2-}$ ) simultaneously incorporated in the structure.<sup>19</sup>

Another interesting observation is the capability of all doping metals to inhibit the growth of cAp nanocrystals. The inhibiting effect of crystal growth is enhanced with the increase in M content, irrespective of the nature of the M (Figure 5). Amorphous calcium phosphates (ACP) are expected at higher M contents. The trend of yielding ACP with the increase at high levels of the M content has been also observed when hydroxyapatite was doped with other metals, i.e.,  $\text{Mg}^{2+}$ .<sup>36</sup> Unlike other works<sup>35</sup> reporting the precipitation of Co-hydroxyapatite particles in carboxylated free solutions in which not only smaller sizes but lower aspect ratios were found, in our experiments the average sizes decrease, whereas the aspect ratio increases due of the strongest inhibition of the growth in the  $(hk0)$  caused by adsorption of citrate in these planes. This finding proves the key role of citrate in shaping the doped nanoparticles.

The growth mechanism of biomimetic nanocrystalline apatites in the presence of citrate has been thoroughly characterized in previous papers.<sup>13,16,17</sup> Following this mechanism, citrate drives the growth pathway via an amorphous precursor stabilizing ACP at the early stage, controlling the amorphous to apatite transformation and the nanocrystal size by adsorption on the  $(10.0)$  face and equivalent planes. Then, citrate influences the growth of nanocrystals by a nonclassical oriented aggregation mechanism. The citrate molecule is too large to be incorporated into the cAp crystal lattice. Therefore, it remains bound to the crystal surface, preferably in the  $(10.0)$  face and equivalent faces. This occurs because  $\text{Ca}^{2+}$  ions in the  $(10.0)$  face, at the two different surface profiles or sublevels,  $(10.0)_1$  and  $(10.0)_2$ , are arranged with a spacing similar to the distance between the centers of the carboxylate groups in citrate.<sup>14</sup> The incorporation of the studied divalent transition metals, as well as  $\text{Na}^+$  and A-, B- carbonate ions substituents most probably takes place during the formation of the amorphous precursor and the progressive amorphous to apatite transformation (from the core to the surface hydrated layer containing the citrate and structural water molecules<sup>13</sup>). In most cases M incorporation occurred in the first 4 h of the experiment, and then the amount of M was kept constant, while in the case of  $\text{Co}^{2+}$  (Figure 2) the M content increased with time, likely during amorphous to cAp transformation, along the whole maturation period. When the M content exceeds a certain threshold (6.5 w/w% calculated in this work) the amorphous calcium phosphate becomes stable. It is worth noting the formation of Mn-doped cAp (Figure S1 of Supporting Information), in which the content of  $\text{Mn}^{2+}$  after the initial precipitation period decreases instead of increasing. The release of M from the solid containing  $\text{Na}^+$  and A- and B-carbonate ion substituents must be a mechanism to facilitate charge compensation and spatial accommodation into the crystalline structure.

The in vitro cell toxicity data confirm that the chemical/electronic modification of these nanocrystals does not

significantly affect cell viability, with the exception of the nanoparticles doped with a high ratio of  $\text{Co}^{2+}$ . Indeed the low toxicity levels are comparable with those observed in the case of cell treatment with undoped nanoparticles. These data, taken together, demonstrate the high biocompatibility degree of these doped nanocrystals and sustain their use as possible biodegradable supports for drug delivery, possibly enhanced by active targeting mediated by probes recognizing specific cell markers.

## 5. CONCLUSIONS

In this paper we have studied the incorporation of  $\text{Mn}^{2+}$ ,  $\text{Co}^{2+}$ , and  $\text{Ni}^{2+}$  in citrate-carbonate-apatite nanocrystals obtained by precipitation from Ca/M/citrate/phosphate/carbonate solutions as well as their influence on crystal growth, microstructure, colloidal stability, and cytotoxicity of precipitated solids.

Besides its influence on the nucleation and crystal growth of biomimetic nanocrystalline apatites, already reported, citrate plays an active role also during the doping process. First, citrate acts as M-complexing agent; second, it controls the activity of hydrated M ions in solution and therefore the extension of the doping process, and third, it protects the M ions against oxidation in solution as well as in doped nanocrystals.

Different trends have been found during our study. First, the growth of nanocrystals is clearly enhanced when temperature is increased and M content is decreased. Second, for similar crystallization conditions the amount of M incorporated normally follows the order  $\text{Mn}^{2+} > \text{Co}^{2+} > \text{Ni}^{2+}$ . Third, the higher the M content, the higher is the aspect ratio ( $L/W$ ) of M-doped compared to undoped cAp nanoparticles. Fourth, when the M content is higher than 6.5 w/w%, the crystallinity (long-range order) of the nanoapatites is lost. Fifth, the colloidal stability of nanoparticles suspensions decreased in the order: undoped, Mn-, Ni-, and Co-doped cAp. Moreover, the cytotoxicity evaluation revealed that the produced Mn- and Co-doped cAp are highly biocompatible at doses comparable to those of undoped cAp, with the exception of those nanoparticles doped with the higher  $\text{Co}^{2+}$  content at the higher doses.

## ■ ASSOCIATED CONTENT

### Supporting Information

The Supporting Information is available free of charge on the ACS Publications website at DOI: 10.1021/acs.cgd.5b01045.

Table S1: Elemental content of Ca, P, Na, Mn, Co, and Ni (% w/w) in the different samples measured by ICP-OES. Table S2: Molar composition of the cationic content in the cAp structure, according to the following formula:  $\text{Ca}_{5-x-y} \text{Na}_{2x} \text{M}_y$ . Table S3: Average size ( $D$ ) of crystal domains along the  $[001]$  and  $[hk0]$  directions, calculated from the microstructural analysis, for all the samples analyzed by PXRD. Table S4: Cell parameters and volume of the hexagonal unit cells of all the samples measured by PXRD. Table S5: Concentrations (mol/L) of the aqueous species considered in the calculations of the activities in Phreeqc. Figure S1) Transition metal content (w/w%) of doped nanoapatites crystallized at Ca/M = 9:1, 37 °C and Ca/M = 5:5, 80 °C. Figure S2: FTIR spectra of the sample Mn(9:1)-96h-80 °C at RT, before and after washing with 0.1 M NaOH solution. Figure S3: Diffractograms of crystallized doped Ap



nanoparticles. Figure S4: Crystal growth of M-doped cAp nanoparticles versus crystallization time. Figure S5: TEM micrograph of the Mn(5:5)-Ap-96h-80 °C sample. Figure S6: (a) Strain versus crystallization time, and (b) strain versus average crystal size. Figure S7: Calculated ionic activities of Ca(citrate)<sup>-</sup>, M-citrate complexes and of the free solvated cations as a function of the temperature, for the (5:5) initial Ca/M molar ratio (PDF)

## AUTHOR INFORMATION

### Corresponding Authors

\*(F.J.M.-C.) E-mail: francisco.martinez@maxlab.lu.se.

\*(J.G.-M.) E-mail: jaime@lec.csic.es.

### Notes

The authors declare no competing financial interest.

## ACKNOWLEDGMENTS

We greatly acknowledge the project Crysfunbio MAT2011-28543 supported by Spanish MINECO and cofunded by FEDER. F.J.M.C. also acknowledges CSIC for his JAE-DOC contract cofunded by European Social Fund. C.M.-B. thanks the ACIISI (Gobierno de Canarias) for a predoctoral fellowship.

## REFERENCES

- (1) Gómez-Morales, J.; Iafisco, M.; Delgado-López, J. M.; Sarda, S.; Drouet, C. *Prog. Cryst. Growth Charact. Mater.* **2013**, *59*, 1–46.
- (2) Iafisco, M.; Margiotta, N. *J. Inorg. Biochem.* **2012**, *117*, 237–247.
- (3) Gruselle, M. *J. Organomet. Chem.* **2015**, *793*, 93.
- (4) Liu, R.; Lal, R. *Sci. Rep.* **2014**, *4*, 5686.
- (5) Zhou, H.; Lee, J. *Acta Biomater.* **2011**, *7*, 2769–2781.
- (6) Cai, Y.; Tang, R. *J. Mater. Chem.* **2008**, *18*, 3775–3787.
- (7) Uskoković, V.; Uskoković, D. *P.J. Biomed. Mater. Res. B Appl. Biomater.* **2011**, *96B*, 152–191.
- (8) Ferraz, M. P.; Monteiro, F. J.; Manuel, C. M. *J. Appl. Biomater. Biomech.* **2004**, *2*, 74–80.
- (9) Dorozhkin, S. V. *Acta Biomater.* **2010**, *6*, 715–734.
- (10) Sadat-Shojai, M.; Khorasani, M.-T.; Dinpanah-Khoshdargi, E.; Jamshidi, A. *Acta Biomater.* **2013**, *9*, 7591–7621.
- (11) Bleek, K.; Taubert, A. *Acta Biomater.* **2013**, *9*, 6283–6321.
- (12) Newcomb, C. J.; Bitton, R.; Velichko, Y. S.; Snead, M. L.; Stupp, S. I. *Small* **2012**, *8*, 2195–2202.
- (13) Delgado-López, J. M.; Iafisco, M.; Rodríguez, I.; Prat, M.; Gómez-Morales, J.; Tampieri, A. *Acta Biomater.* **2012**, *8*, 3491–3499.
- (14) Hu, Y.-Y.; Rawal, A.; Schmidt-Rohr, K. *Proc. Natl. Acad. Sci. U. S. A.* **2010**, *107*, 22425–22429.
- (15) López-Macipe, A.; Gómez-Morales, J.; Rodríguez-Clemente, R. *Adv. Mater.* **1998**, *10*, 49–53.
- (16) Delgado-López, J. M.; Frison, R.; Cervellino, A.; Gómez-Morales, J.; Guagliardi, A.; Masciocchi, N. *Adv. Funct. Mater.* **2014**, *24*, 1090–1099.
- (17) Iafisco, M.; Ramírez-Rodríguez, G. B.; Sakhno, Y.; Tampieri, A.; Martra, G.; Gómez-Morales, J.; Delgado-López, J. M. *CrystEngComm* **2015**, *17*, 507–511.
- (18) Rodríguez-Ruiz, I.; Delgado-López, J. M.; Durán-Olivencia, M. A.; Iafisco, M.; Tampieri, A.; Colangelo, D.; Prat, M.; Gómez-Morales, J. *Langmuir* **2013**, *29*, 8213–8221.
- (19) Šupová, M. *Ceram. Int.* **2015**, *41*, 9203–9231.
- (20) Kolmas, J.; Groszyk, E.; Kwiatkowska-Różycka, D. *BioMed Res. Int.* **2014**, *2014*, No. 178123.
- (21) Burnell, J.; Teubner, E.; Miller, A. *Calcif. Tissue Int.* **1980**, *31*, 13–19.
- (22) Boanini, E.; Gazzano, M.; Bigi, A. *Acta Biomater.* **2010**, *6*, 1882–1894.

- (23) Mayer, I.; Jacobsohn, O.; Niazov, T.; Werckmann, J.; Iliescu, M.; Richard Plouet, M.; Burghaus, O.; Reinen, D. *Eur. J. Inorg. Chem.* **2003**, *2003*, 1445–1451.
- (24) Tank, K. P.; Chudasama, K. S.; Thaker, V. S.; Joshi, M. J. *Nanopart. Res.* **2013**, *15*, 1644–1655.
- (25) Ignjatović, N.; Ajduković, Z.; Savić, V.; Najman, S.; Mihailović, D.; Vasiljević, P.; Stojanović, Z.; Uskoković, V.; Uskoković, D. *J. Mater. Sci.: Mater. Med.* **2013**, *24*, 343–354.
- (26) Finiels, A.; Fajula, F.; Hulea, V. *Catal. Sci. Technol.* **2014**, *4*, 2412–2426.
- (27) Chan, F. L.; Tanksale, A. *Renewable Sustainable Energy Rev.* **2014**, *38*, 428–438.
- (28) Gruselle, M. *J. Organomet. Chem.* **2015**, *793*, 93–101.
- (29) Boukha, Z.; Kacimi, M.; Pereira, M. F. R.; Faria, J. L.; Figueiredo, J. L.; Ziyad, M. *Appl. Catal., A* **2007**, *317*, 299–309.
- (30) Parkhurst, D. L.; Appelo, C. A. J. in *U.S. Geological Survey Techniques and Methods* 2013, Book 6, Chapter A43, 497 pp, available only at <http://pubs.usgs.gov/tm/06/a43/>.
- (31) (a) Rodríguez-Carvajal, J. *Phys. B Condens. Matter* **1993**, *192*, 55–69. (b) Rodríguez-Carvajal, J. *Commission on Powder Diffraction (IUCr) Newsl.* **2001**, *26*, 12.
- (32) Iafisco, M.; Marchetti, M.; Gómez-Morales, J.; Hernández-Hernández, M. A.; García-Ruiz, J. M.; Roveri, N. *Cryst. Growth Des.* **2009**, *9* (11), 4912–4921.
- (33) Boulif, A.; Louer, D. *J. Appl. Crystallogr.* **2004**, *37*, 724–731.
- (34) Wilson, R. M.; Elliott, J. C.; Dowker, S. E. P.; Smith, R. I. *Biomaterials* **2004**, *25*, 2205–2213.
- (35) Veselinovic, L.; Karanovic, L.; Stojanovic, Z.; Bračko, I.; Markovic, S.; Ignjatovic, N.; Uskokovic, D. *J. Appl. Crystallogr.* **2010**, *43*, 320–327.
- (36) Tampieri, A.; Celotti, G.; Landi, E.; Sandri, M. *Key Eng. Mater.* **2004**, *264–268*, 2051–2054.